



Exceptionally high spallation strength for a high-entropy alloy demonstrated by experiments and simulations



Daniel Thürmer^a, Shiteng Zhao^b, Orlando R. Deluigi^c, Camelia Stan^d, Iyad Alabd Alhafez^e, Herbert M. Urbassek^e, Marc A. Meyers^f, Eduardo M. Bringa^{c,g}, Nina Gunkelmann^{a,*}

^a Clausthal University of Technology, Institute of Applied Mechanics, Adolph-Roemer Str. 2A, Clausthal Zellerfeld 38678, Germany

^b Materials Science and Engineering, University of California, Berkeley, CA, United States

^c CONICET and Faculty of Engineering, University of Mendoza, Mendoza 5500, Argentina

^d National Ignition Facility & Photon Science, Lawrence Livermore National Laboratory, 7000 East Avenue, Livermore CA 94550, United States

^e Physics Department and Research Center OPTIMAS, University Kaiserslautern, Erwin-Schrödinger-Straße, D-67663 Kaiserslautern, Germany

^f Mechanical and Aerospace Department, Univ. of California San Diego, La Jolla, CA 92093, United States

^g Centro de Nanotecnología Aplicada, Universidad Mayor, Santiago, Chile

ARTICLE INFO

Article history:

Received 7 August 2021

Received in revised form 13 October 2021

Accepted 29 October 2021

Available online 2 November 2021

Keywords:

Molecular dynamics
Shock waves
Spallation
High-entropy alloys

ABSTRACT

High-entropy alloys are materials with an increasing number of technological applications. Amongst them, the Cantor alloy, FeMnCoCrNi, shows desirable mechanical properties at normal loading conditions. In this study we focus on the performance of the Cantor alloy at the ultra-high deformation rates of shock waves. We study shock-induced spallation using both experiments and atomistic simulations. Experimental loading is achieved using high power laser, with VISAR to obtain velocity profiles and spall strength, followed by transmission electron microscopy of the recovered samples. Molecular Dynamics (MD) simulations of shock-induced spallation are compared with experiments. Both experiments and simulations show a high spall strength which would be beneficial for certain applications, with experiments giving ~8 GPa at $\sim 10^7 \text{ s}^{-1}$ and MD giving almost ~30 GPa at $\sim 10^9 \text{ s}^{-1}$. The difference between experiments and simulations can be explained by the difference in strain rate. Post-mortem analysis of the experimental samples shows nanotwins near the spall plane, while MD simulations show a highly disordered region giving rise to void nucleation and spall during loading.

© 2021 Elsevier B.V. All rights reserved.

1. Introduction

High-entropy alloys (HEAs) are a novel class of materials that are formed by mixing equal or relatively large proportions of several elements [1–4,5]. They may exhibit both high strength and large ductility [2,6–9]. One of the best known HEAs is the Cantor alloy, an equiatomic CoCrFeMnNi alloy [10], which forms a single-phase face-centered cubic (fcc) solid solution. Although the mechanical properties of HEAs have been well documented in the literature, their high-strain-rate behavior is relatively poorly understood. Shock-wave loading leads to high pressures, high strain rates, and temperature increase, and can be relevant for some technological applications. In addition, samples recovered after loading might present desirable features, like additional hardening [11]. Shock-induced phase transformations are of major interest for materials

technology, where new materials can be created for machining purposes.

These phase transformations are highly influenced by temperature, pressure, and the addition of further elements, as shown for a body-centered cubic (bcc) Al₂CoCrFeNi HEA [12]. Regarding the Cantor alloy, Jiang et al. performed gas-gun experiments and demonstrated that the yield strength increased significantly with strain rate, exceeding values for many austenitic steels [13]. Hopkinson bar experiments showed shear band formation only after extremely large shear strains [2], with outstandingly high fracture toughness and resistance to shear-band formation under dynamic loading [2]. Recently, Kawamura et al. have shown that the critical resolved shear stress for the Cantor alloy increases with decreasing temperature, without exhibiting any significant inertia effects at cryogenic temperatures [14]. The variation of yield strength with strain rate under dynamic compression was recently shown to be much larger than under quasi-static compression, for strain rates up to 10⁴/s [15].

When shock waves reach the free surfaces of the sample they are reflected as release waves and their superposition results in a tensile

* Corresponding author.

E-mail address: nina.gunkelmann@tu-clausthal.de (N. Gunkelmann).

pulse. If the magnitude of the tensile stress exceeds a critical value, the spall strength, spall occurs [16,17]. Several studies have shown that spall strength depends on strain rate [18,19]. The spall behavior and the microstructure of recovered samples, however, needs further discussion for HEAs, because most of the atomistic studies and experiments about spall response deal with single-element fcc [20–23] or bcc metals [18,24]. The spall behavior of shocked duplex stainless steels has been studied by electron backscatter diffraction and x-ray computed tomography [25]. Recently, Zhao et al. have subjected CrMnFeCoNi HEAs to severe plastic deformation through swaging followed by either quasi-static compression or dynamic deformation in shear and found that amorphization occurs in the vicinity of the shear bands, via the population of stacking faults, twins and hcp phases [26]. Xie et al. [27] have studied hydrogen induced spallation in CrMnFeCoNi HEA under plate impact loading and found that hydrogen-retarded nucleation of micro-voids can be attributed to hydrogen-vacancy complexes with high migration energy, while formation of nano-twins with high resistance reduces their growth rate.

In general, spall can be influenced by shock-induced phase transitions, for instance for Fe [28]. The Cantor alloy can display an fcc to hexagonal close-packed (hcp) transition [29], which can influence spall strength. It has been shown that Mo doping [30] and large deviatoric stress induced by the non-hydrostaticity of the pressure medium [31] can promote this phase transition.

In this paper, we present experiments and simulations of shock-wave loading and spall of the equiatomic CoCrFeMnNi fcc Cantor alloy. High-power lasers are used for loading, as detailed in [17]. The Velocity Interferometry System for Any Reflector (VISAR) is used to obtain back-surface velocities and deduce spall strength. Recovered samples are analyzed with transmission electron microscopy (TEM). Microstructure during loading can be significantly different from the microstructure in the recovered sample, and atomistic simulations can provide helpful information [32,33]. Our MD simulations provide not only spall strength, but details on microstructure during spall. We also discuss the difference between experiments and simulations in terms of strain rate.

2. Methods

2.1. Experimental methods

The HEA sample was an fcc polycrystal with a grain size of around 100 micrometers, and analysis of these samples was presented by Li et al. [2].

Nanosecond pulsed laser-driven shock experiments were conducted at the Omega laser facility [34] with a nominal square pulse duration of 1 ns, to investigate the deformation and spall mechanism of the Cantor alloy. The 352 nm wavelength laser was defocused to a 3 mm spot to ensure the planarity of the shock front. Laser energy ranging from 100 to 200 J was deposited onto the target package with a 20 μm polystyrene ablator followed by the Cantor alloy. The high energy density laser ablates the polystyrene layer into plasma, leading to rapid volume expansions and launching a strong stress (shock) wave into the subsequent HEA. VISAR experiments were performed to determine the free surface velocity of the shocked target as a function of time, which can be used to extract the spall strength of the material as follows:

$$\sigma_{\text{spall}} = \frac{1}{2} \rho_0 c_0 \Delta U, \quad (1)$$

where σ_{spall} is the spall strength. ρ_0 , and c_0 are the initial density and bulk sound velocity of the material, respectively. $\Delta U = u_{\text{max}} - u_{\text{pull-back}}$ is the so-called "pull-back" signal, which can be measured from the free surface VISAR experiments. We used a sample thickness of 100 μm for the VISAR experiments. Note that the sensitivities of the

VISAR measurement come from the time window of the streak camera. In our case it is 50 ns, which is sufficient to capture the shock break-out and pull-back in our sample.

To understand the microscopic spall mechanisms, separate shock recovery experiments were conducted where the shocked sample was soft recovered in a tube filled with glass fibers and then characterized by multi-scale electron microscopy techniques. A detailed review of the deformation and failure in extreme regimes by high-energy pulsed lasers is given in [17].

2.2. Simulation methods

The public-domain molecular dynamics code LAMMPS [35] was used in this paper to perform the simulations.

The CoCrFeMnNi HEA atoms are distributed randomly on the lattice points of an fcc structure with equal ratios of 20%, with a lattice constant $a_0 = 0.3595$ nm. The orientation is [001], [010], [100]. Our sample contains approximately 2 million atoms and has a size of $18 \times 18 \times 72$ nm³, but some larger samples were also simulated for selected cases.

We used the modified embedded atom model (MEAM) potential by Choi et al [36]. The potential has been validated by formation and mixing enthalpies and lattice constants of solid phases. It has been successfully used in atomistic studies on the influence of plasticity under compression and tension [37] as well as indentation [38]. The potential reproduces the formation of micro-twins during low temperature deformation [36]. Choi et al. calculated the energy difference between hcp and fcc structure to estimate the stacking fault energy (SFE). They found that a higher stability of hcp yields a low SFE and eventually leads to the easy formation of micro-twins in the HEA [36]. Here, we find an enthalpy difference of hcp/fcc of 0.0084 eV/atom at 0 K which is in perfect agreement with the result by Choi et al. [36].

This potential also gives reasonable values for elastic constants C_{11} and C_{12} , but C_{44} is too low, as it can be seen in Table 1, when comparing with experiments and ab-initio simulations at zero pressure. We note that our data differ considerably from the values published in [37] for the same interaction potential; our data were obtained using the ELASTIC_T module within LAMMPS. The elastic constants behave well under deformation, as shown in Fig. 1. Using the Cauchy stability criteria, the fcc solid is stable in the range (-30 , 100) GPa of hydrostatic pressure. The Cauchy pressure is positive, unlike experimental and ab-initio results. A positive Cauchy pressure is usually associated with isotropic metallic-like bonding, while negative values are associated with rather covalent bonding [39].

We relaxed the MD sample using an isothermal-isobaric (NPT) ensemble at a temperature of 1 mK and zero pressure for 100 ps. We chose this low temperature because it allows us to identify defects more easily. Test runs with higher initial temperatures showed no change in the overall material behavior during shock and release. After relaxation, a microcanonical NVE ensemble is used, and shock wave simulations are conducted using this initial low temperature in order to minimize thermal noise and optimize structure identification.

Table 1

Single crystal elastic constant comparison of CoCrFeMnNi at 0 GPa. The Cauchy pressure $P_C = C_{12} - C_{44}$ obtained differs in our calculations with MD.

	C_{11} [GPa]	C_{12} [GPa]	C_{44} [GPa]	P_C [GPa]
Experiment[14]	192	118	122	-4
Calculation[43]	201	97	147	-50
Calculation[44]	236	146	187	-41
Calculation[45]	217	113	184	-71
Calculation[46]	189.9	123.8	139.2	-15.4
MD	210	154	72	82

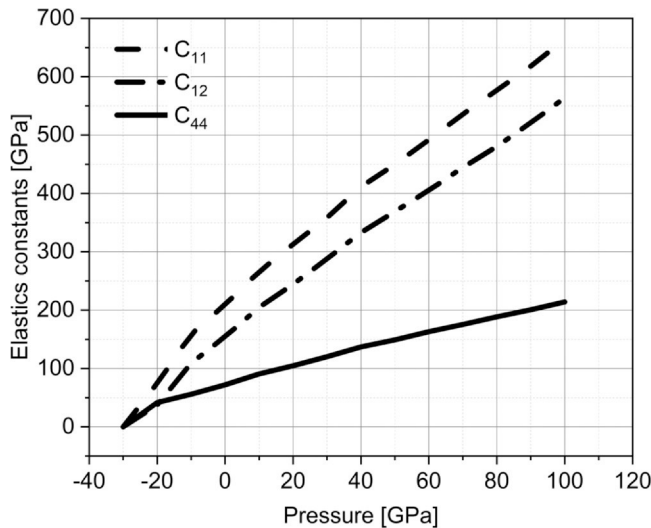


Fig. 1. Elastic constants (C_{11} , C_{12} and C_{44}) calculated in the range of -30 – 100 GPa at 300 K .

Shock waves are generated with a piston-driven algorithm [40,41] by giving the atoms in a thin slab (thickness a_0) on one side of the sample a certain particle velocity U_p in km/s along the z direction. These piston atoms are not subjected to the forces of the surrounding atoms. We apply periodic boundary conditions in x and y direction and free boundaries along the shock direction.

We consider piston velocities varying from $U_p = 0.5$ to $U_p = 1.6$ km/s. The piston velocity is increased linearly from 0 to U_p during a ramp loading time of 0.2 ps, and then the piston moves with a constant velocity until immediately before the first reflection of the wave. We also performed a simulation with a longer ramp time of 2 ps in order to decrease the strain rate. This reflection occurs at 12 ps for $U_p = 0.5$ km/s, 11 ps for $U_p = 0.8$ km/s and 10 ps for $U_p = 1.6$ km/s. These holding times ensure relatively stable shock wave profiles. After this time, piston velocity is decreased linearly to 0 over 5 ps. Afterwards, the simulation is continued until a total simulation time of 55 ps. These loading profiles lead to unloading waves from the back surface due to the reflecting shock, and also from the front surface when the piston stops. For comparison, we also performed a simulation where the piston speed remained constant for a total time of 40 ps.

To evaluate the simulation results we determined several material properties as a function of depth z . These profiles were determined by dividing the sample into 200 bins corresponding to thicknesses varying between 0.35 nm and 0.51 nm. We measure the velocity along z , v_z , stress in z direction, σ_{zz} , and the shear stress, τ_{shear} . The latter is defined as

$$\tau_{shear} = \frac{1}{2}(\sigma_{zz} - \sigma_{trans}), \quad (2)$$

where σ_{ij} denote the components of the stress tensor, and the transverse pressure is defined as

$$\sigma_{trans} = \frac{1}{2}(\sigma_{xx} + \sigma_{yy}). \quad (3)$$

For visualization of the atomistic configurations we use the free software tool OVITO [42], with Polyhedral Template Matching (PTM) and RMSD=0.2 for structure identification.

3. Results

3.1. Experimental results

The spall strength of a shocked sample can especially at higher stress be estimated from the VISAR back-surface velocity using Eq.

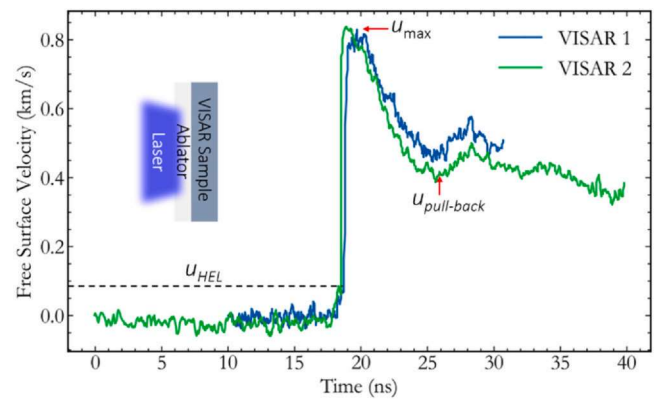


Fig. 2. Free surface velocity profile of the Cantor alloy subjected to a laser-induced shock. Two independent measurements (VISAR 1 and 2) give nearly the same ΔU . Inset shows the schematic experimental set-up.

(1). The spall strength of the material is determined to be around 8 GPa. There are sources of error coming from the quality of VISAR signals, which varies amongst experiments. Note that the spall strength typically also depends on the grain size. A theory of cavitation was derived to explain this grain size dependence of the spall strength [47].

A strain rate in the order of 10^7s^{-1} can be estimated from the following equation where u_{\max} and u_{\min} are the peak and pull back free surface velocity, Δt being the pulse duration (1 ns) and c is the sound velocity:

$$\dot{\epsilon} = \frac{(u_{\max} - u_{\min})}{\Delta t \times 2c} \quad (4)$$

From the VISAR profile in Fig. 2 we can also estimate the peak shock pressure in the sample:

$$\sigma_{peak} = \frac{1}{2}\rho_0 u_{\max} U_s, \quad (5)$$

where $\rho = 7.856\text{ g/cm}^3$ is the density of the material, u_{\max} is the maximum free surface velocity and is approximately half the particle velocity u_p , and U_s is the shock velocity, which can be correlated with the particle velocity via the shock Hugoniot, $U_s = c_0 + su_p$. Jiang et al. [13] reported that $c_0 = 4.5$ km/s and $s = 1.39$ for the Cantor alloy. Therefore, the peak shock stress is around 41.3 GPa in our experiment. This peak stress value is remarkably high for fcc metals, which have values below 5 GPa at this strain rate, and it matches the spall strength of strong bcc metals like Ta.

Fig. 3(a) shows a crater at the front surface, approximately of the size of the laser spot, with partial spall at the back surface. Fig. 3(b) shows cracks and microvoids in the spall region. Microscopy around the microvoids in Fig. 3(c) shows grain boundary and lattice rotations. High resolution transmission electron microscopy (TEM) of the recovered material indicates that the Cantor alloy deformed predominately by nanoscale mechanical twinning at elevated strain rates, as shown in Fig. 3(d). The high density of nanotwins provides a sustainable work-hardening rate and therefore contributes to the high strength of the material. The rationale is two-fold: (1) the Cantor alloy exhibits an extremely low stacking-fault energy which promotes mechanical twinning, especially at higher stress levels; and (2) mechanical twinning is further facilitated by the high strain rate, which prefers twinning over dislocation slip as thermal activation is largely reduced [48]. Note that such behavior is analogous to the cryogenic response of the Cantor alloy where mechanical twinning also prevails as the deformation mechanism. Both under cryogenic conditions and in high-strain-rate regimes, an athermal mechanism such as twinning is favored. This is supported by recent MD simulations of nanocrystalline samples of the Cantor alloy under

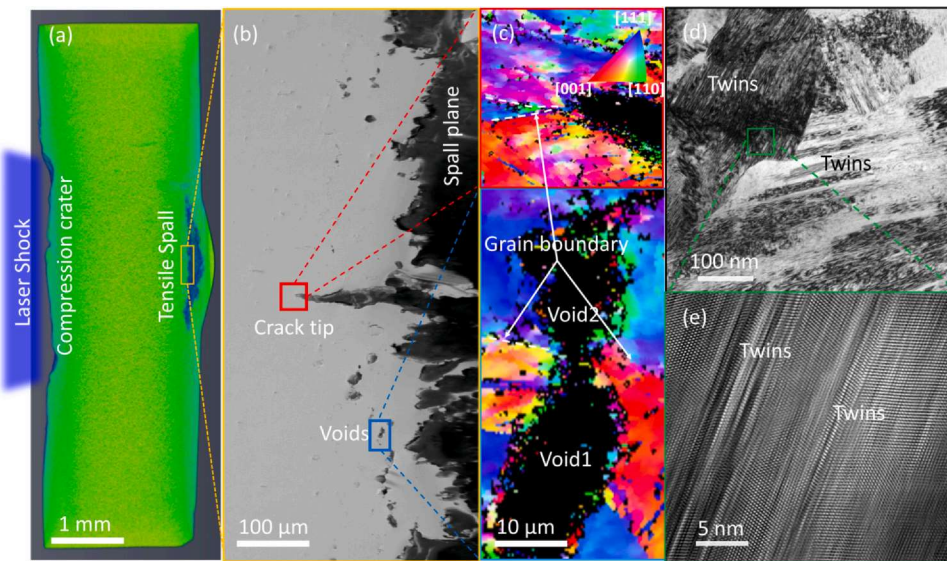


Fig. 3. Multiscale microstructure characterization of the laser-shocked Cantor alloy: (a) x-ray computed tomography of the shocked recovered sample with crater on the laser-facing surface and spall fracture close to the rear surface; (b) secondary electron micrograph of the vicinity of the spall plane; (c) electron backscattered diffraction map of the microvoids along the grain boundaries and (d,e) TEM images of the nanoscale twin boundaries produced by shock deformation.

tension [49]. This post-mortem study of recovered samples is indicative of the deformation mechanism during loading, but additional diagnostics like in-situ X-ray diffraction would be required to better ascertain the roles of twinning and dislocations during loading [33,50].

3.2. Simulation results

Shock propagation occurs as expected for an fcc material with [001] orientation. An elastic wave is followed by a plastic wave responsible for the nucleation of stacking faults, dislocations and twins. The Hugoniot Elastic limit (HEL) for the perfect single crystal is around 7 GPa. Fig. 4 displays the changes induced in our sample by the passage of the shock and release wave using different piston velocities for our MD simulations. Void nucleation and growth associated with partial spall occur when the back surface release encounters the front surface pulse.

Stacking faults (SF) are detected as a double layer of hcp atoms, while twin boundaries appear as a single layer of hcp atoms. However, 3D clusters of atoms with hcp phase were not detected, indicating that the material mostly retained fcc structure during loading, except for the strongest shock studied here, as shown in Fig. 4(c). In all cases, some isolated bcc atoms are observed, which could be a result of the large uniaxial distortion of the fcc lattice and the thermal noise and not necessarily be representative of a true bcc phase. At the spall region, the material disorders and visual inspection indicates amorphization due to tensile stress and heating, identified as an “unknown” phase by PTM, and this is where voids nucleate. Similar behavior has been reported in simulations of Cu spall [18,51]. Note that we observe in our simulations that the temperature at the spall surface rises considerably to values close to the melting temperature. We see from Fig. 4 that the spall time decreases with increasing piston velocity due to the increased wave speed.

For 0.5 km/s, Fig. 4(a), there is limited plasticity in the sample, including SFs and dislocations near the spall region. The spall surface is more clearly defined for 0.8 km/s, Fig. 4(b). This sample exhibits significant shock plasticity by dislocations, SFs and twins, but most of them disappear upon the fast unloading. Annihilation of shock-induced dislocations has been reported for Cu [32], and twin annihilation has been reported for experiments and simulations of bcc Ta

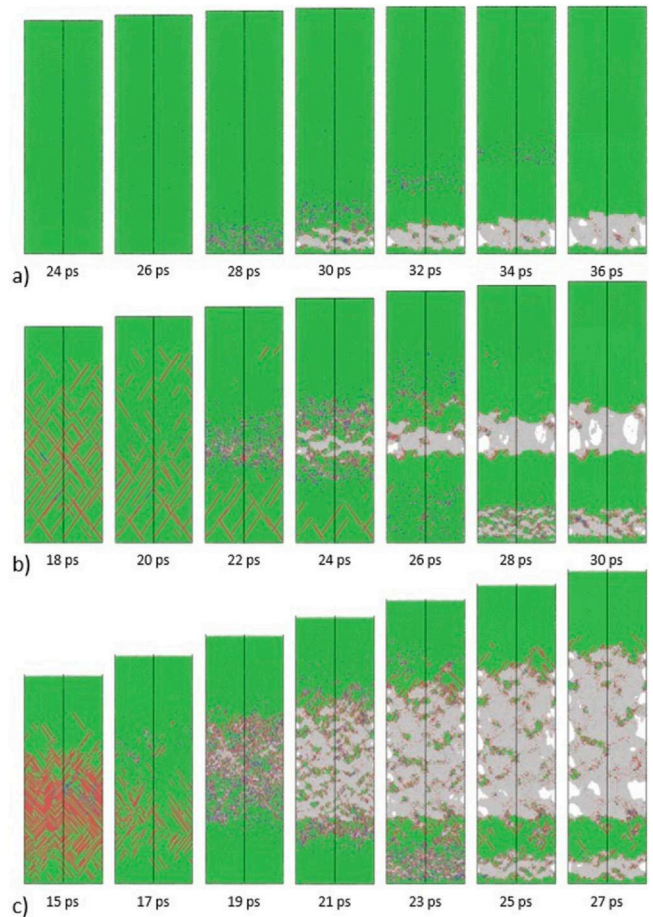


Fig. 4. Snapshots of the sample for piston velocities of 0.5 km/s (a), 0.8 km/s (b) and 1.6 km/s (c) at different time steps. Local atomic structures are identified by PTM within OVITO [42]. Green: fcc; red: hcp; blue: bcc; light grey: other. The shock propagates from bottom to top.

[50]. For the 1.6 km/s shock, Fig. 4(c), the spallation process has started at 19 ps with the nucleation of a series of small voids near the center of the sample, but later on a second spall surface appears near

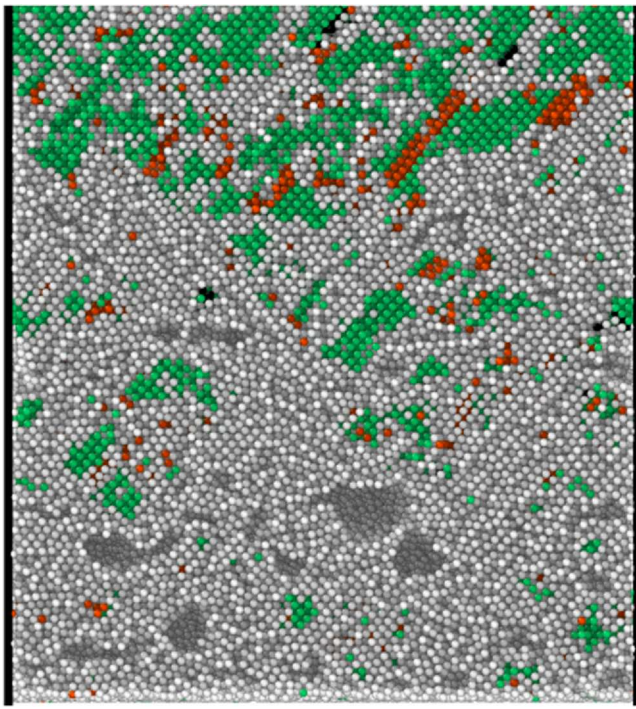


Fig. 5. Zoom of the spall region of length 20 nm (at position 69 nm) for a piston velocity of 1.6 km/s after 19 ps. Green: fcc; red: intrinsic stacking faults; black: coherent twin boundaries; light grey: other. The shock wave propagated from bottom to top. Structures are analyzed using the Crystal Analysis Tool [52].

the piston. A zoom of the spalled region is given in Fig. 5 showing voids and stacking faults.

The large number of stacking faults and twins observed in MD simulations (see Fig. 4c and Fig. 5) is consistent with the nanotwinning observed in the recovered experimental samples, since slower unloading might help retaining more microstructure than in our MD simulations. Experiments also indicate the possibility of fcc to hcp transformation for the pressure range studied here [31], based on the microstructure of recovered samples. We use small samples, with a stress history which involves extremely fast strain rates for both loading and unloading, and it is therefore difficult to compare our simulated unloaded samples with recovered experimental samples.

We evaluate the dynamics within the shock and release wave by showing its spatially resolved characteristics for various times in Fig. 6. We display the velocity along the shock direction, the pressure component parallel to the shock direction, and the shear stress. We observe a clear shock front for all piston velocities. The resulting shock pressures in Fig. 6 are 20, 34 and 70 GPa. Note that due to the superposition of incident and reflected wave the maximum tensile stress is larger than the incident shock pressure. Spall occurs at times greater than 10 ps after release, depending on the piston velocity. As expected, spall time decreases with increasing piston velocities as a consequence of the increase of shock-wave speed with piston speed. The spall stress is identified as the minimum values of σ_{zz} , falling in the range 23–30 GPa. The weaker shock leads to a higher value of spall strength, partly because heating is lower for that shock and spall strength decreases with temperature [51].

The model by Grady [16] is often used to estimate an upper limit of the spall strength:

$$\sigma_{Uspl} = (B_0 U_{coh} / 8V_0)^{0.5}, \quad (6)$$

where B_0 , U_{coh} , and V_0 are the bulk modulus, cohesive energy and specific volume at zero pressure. For the HEA studied here, using simulation values $B_0 = 173$ GPa, $U_{coh} = 4.05$ eV, and a lattice

parameter $a_0 = 0.3595$ nm, gives $\sigma_{Uspl} = 35$ GPa, as the ultimate spall strength. Therefore, this material is comparable to bcc metals Ta [18] and Fe [53], whose ultimate spall strengths are 33 GPa and 34 GPa respectively. This spall strength value is also close to the tensile pressure at which the elastic constants become zero for the HEA in Fig. 1.

The MD values for spall strength can be compared to the experimental spall strength of around 8 GPa at a much smaller strain rate, $\sim 10^7 \text{s}^{-1}$. They are also consistent with recent experimental findings by Kawamura *et al.* [14] showing large ductility. Note that these authors have not observed any twin boundaries at room temperature. Shear stress is smallest for the strongest shock, consistent with increased relaxation by extensive plasticity.

The shear stress shows no fluctuations for our weakest shock with piston velocity 0.5 km/s and no indication of plasticity is seen before spall occurs. In contrast, for the strongest shock, we see a rough shear stress profile at 15 ps before spallation starts due to the high number of stacking faults in the sample.

As mentioned above, we also studied a pure shock simulation where the piston was held at 1.6 km/s. The results are consistent with the release simulation exhibiting the same morphological behavior and spall strength. However, the spallation occurs later, as expected, because the overall tensile pulse is slightly weaker when the piston is not released. Note that we also ran simulations with a larger sample that was two times longer than the samples above using the same simulation procedure. The spallation profile here is very similar and it results in a spall stress of about 23 GPa, as seen in Fig. 7.

Our MD simulations for a single crystal will give an upper bound to the spall strength for polycrystals, given that grain boundaries might lower the required spall stress [54]. Large scale atomistic simulations can only reach grain sizes below 50 nm [11,55], and they are usually close to 10 nm [28]. Therefore, they will not represent the conditions for the experimental polycrystals used here, with grain size of 100 μm , 10^4 larger than typical MD simulations.

4. Discussion and conclusions

In this paper we have presented both experiments and simulations of shock wave loading and spall in the equiaxed Cantor high-entropy alloy, FeCrMnNiCo.

Experimental spall strength is ~ 8 GPa at $\sim 10^7 \text{s}^{-1}$ and MD spall strength is ~ 30 GPa at $\sim 10^9 \text{s}^{-1}$. This can be compared to the theoretical ultimate spall strength [16], which is 34 GPa for this HEA. Experimental and MD differences are reasonable because an analytical model of the relationship between the spall strength and strain rate of solids using molecular dynamics simulations describes the spall strength as a power law of the strain rate with exponent 0.2 for Cu [56]. As an fcc material copper is expected to exhibit a similar strain-rate dependence in comparison to the Cantor alloy. In Fig. 8 we plot the spall strength versus strain rate for the Cantor alloy, Cu, Ta and Fe, where the data for the Cantor alloy are fitted by a power law with exponent 0.2. We observe that our spall strength is higher than the one of recent experiments by Xie *et al.* [27], showing a spall strength of around 2.5 GPa at a lower strain rate of $\sim 10^5 \text{s}^{-1}$. The power law dependence also agrees with recent experimental results for laser-shock compression experiments in Cu [19]. Our results can be compared to laser-shock compression experiments for Ta [18] and Fe [53], which display a smaller strain-rate dependence for the spall strength.

The experimental spall strength for this fcc HEA is extremely large (8 GPa), and comparable with the spall strength of a strong bcc material like Ta at the same strain rate of $10^7/\text{s}$ [18]. The ultimate spall strengths of Ta and Fe are reached only near $10^{12}/\text{s}$, because the strain rate exponent is around 0.1 [53,54]. However, for fcc materials this exponent is expected to be higher, around 0.2, as noted above. In

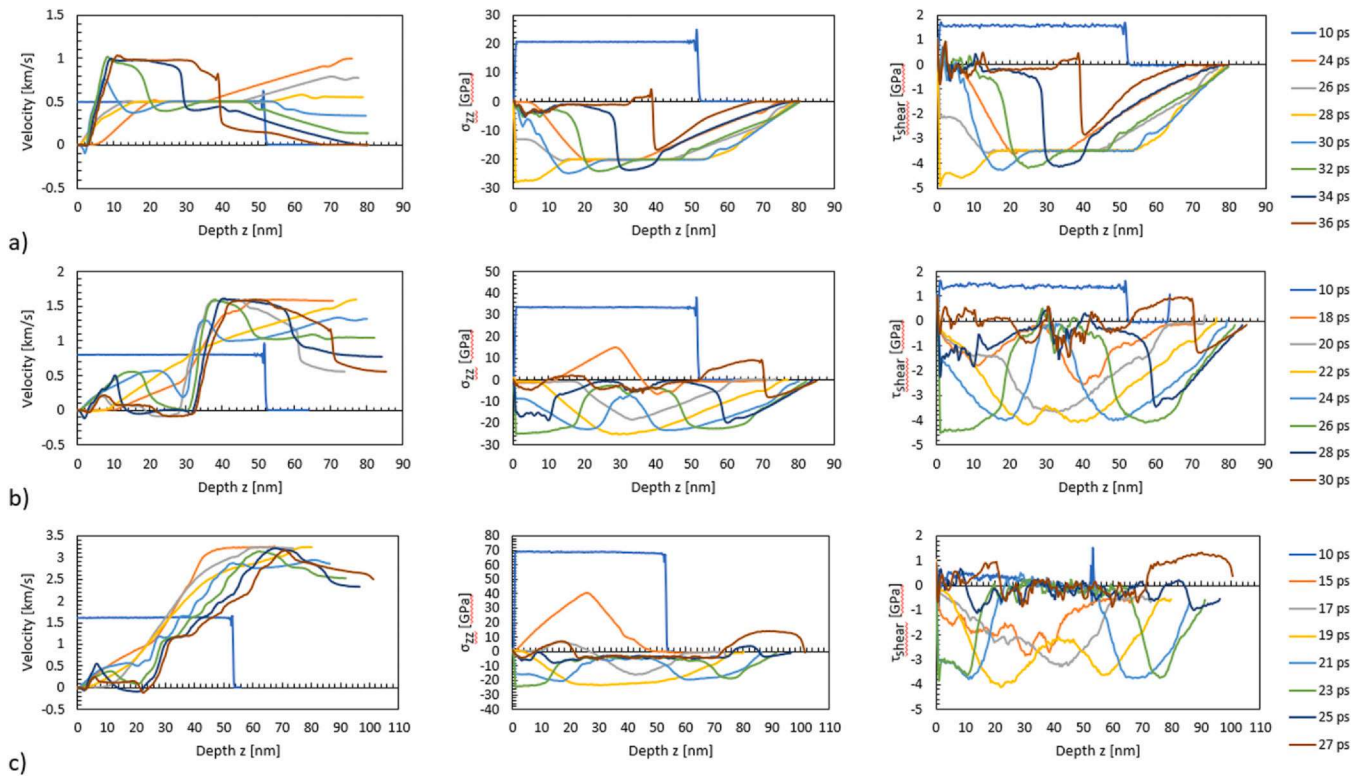


Fig. 6. Spatial profiles of the atom velocity in z direction, v_z , the pressure components parallel to the shock wave propagation direction, σ_{zz} and the shear stress, Eq. 2, for several piston velocities: 0.5 km/s (a), 0.8 km/s (b), 1.6 km/s (c).

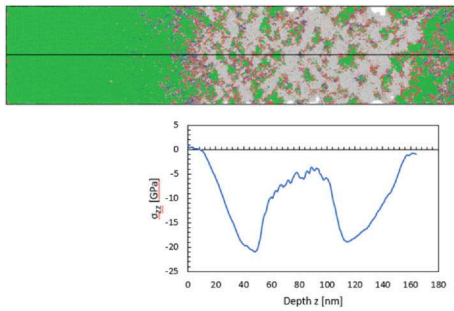


Fig. 7. Spatial profile of the sample with size $(18 \times 18 \times 144)$ nm 3 at 38 ps with a piston velocity of 1.6 km/s. Local atomic structures are identified by PTM within OVITO [42]. Green: fcc; red: hcp; blue: bcc; light grey: other. The shock wave propagated from left to right, along the z-direction.

this case, the ultimate spall strength might be reached at lower strain rates than those of Ta, as we explore in these simulations, and could be reached experimentally by laser-shocks. One possible reason for the high spall strength is the homogeneous composition of the alloy, with a clear absence of second-phase particles and/or segregation at the grain boundaries. These effects are known to considerably reduce the spall strength. From the high spall strength one also expects a strong hardening capacity of the Cantor alloy. A reason is the variety of nanostructured heterogeneities in the HEA. For example, the high density of nanotwins provides a sustainable work-hardening rate. In addition, precipitation hardening due to the interaction of precipitates with dislocations could provide increased capability of strain hardening.

The analysis of the experimental samples shows nanotwins near the spall plane, while our atomistic simulations exhibit an amorphous region giving rise to void nucleation and spall during loading.

There are novel multiscale simulation techniques which can help determining spall strength and could be parametrized to study HEA

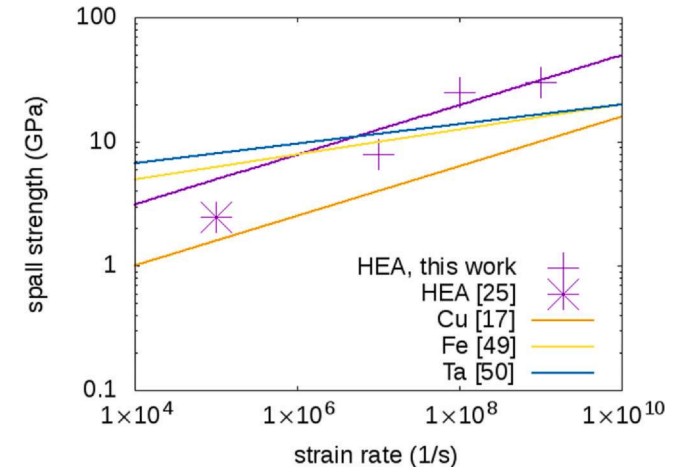


Fig. 8. Spall strength versus strain rate for the Cantor alloy, Cu, Ta and Fe. The data for the Cantor alloy is fitted by a power law of the form $a\dot{\epsilon}^{0.2}$ (purple line) with the strain rate $\dot{\epsilon}$ and fit value $a = 0.49$ GPa s $^{0.2}$. Included are the fits by Coakley et al. for Cu [19], Righi et al. [53] for Fe and Remington et al. for Ta [54] single crystals.

[57]. Future experiments using the same strain rates which are possible in atomistic simulations will shed additional light on the mechanical properties of shocked HEA.

CRediT authorship contribution statement

Daniel Thürmer: Investigation, Formal analysis, Data curation, Software (MD simulations and analysis), Writing – review & editing.
Shiteng Zhao: Investigation, Formal analysis, Data curation, Experiments, Writing – original draft, Writing – review & editing.
Orlando R. Deluigi: Investigation, Formal analysis. **Camelia Stan:** Investigation, Writing – review & editing. **Iyad Alabd Alhafiez:**

Investigation, Software (Sample generation). **Herbert M. Urbassek:** Funding acquisition, Conceptualization, Methodology, Writing – review & editing. **Marc A. Meyers:** Conceptualization, Writing – review & editing. **Eduardo M. Bringa:** Funding acquisition, Conceptualization, Methodology, Investigation, Writing – original draft, Writing – review & editing. **Nina Gunkelmann:** Funding acquisition, Conceptualization, Methodology, Investigation, Writing – original draft, Writing – review & editing.

Declaration of Competing Interest

The authors declare that they have no known competing financial interests or personal relationships that could have appeared to influence the work reported in this paper.

Acknowledgements

DT and NG greatly appreciate the financial support from Simulation Science Center Clausthal / Göttingen. EMB and OD thank support from UNCuyo SIIP grant 06/M035, and from PICTO-UUMM-2019-00048. IAA and HMU acknowledge funding by the Deutsche Forschungsgemeinschaft (DFG, German Research Foundation) – project number 172116086-SFB 926 and computation at the High Performance Cluster Elwetritsch (RHRK, TU Kaiserslautern, Germany). The experimental portion of this work was performed under the auspices of the U.S. Department of Energy by Lawrence Livermore National Laboratory under Contract DE-AC52-07NA27344, and is identified as LLNL-JRNL-825521-DRAFT.

References

- [1] D.B. Miracle, O.N. Senkov, A critical review of high entropy alloys and related concepts, *Acta Mater.* 122 (2017) 448–511, <https://doi.org/10.1016/j.actamat.2016.08.081>
- [2] Z. Li, S. Zhao, R.O. Ritchie, M.A. Meyers, Mechanical properties of high-entropy alloys with emphasis on face-centered cubic alloys, *Prog. Mater. Sci.* 102 (2019) 296 – 345, <https://doi.org/10.1016/j.pmatsci.2018.12.003>, <http://www.sciencedirect.com/science/article/pii/S0079642518301178>.
- [3] Y. Zhou, D. Zhou, X. Jin, L. Zhang, X. Du, B. Li, Design of non-equiautomic medium-entropy alloys, *Sci. Rep.* 8 (2018) 1–9, <https://doi.org/10.1038/s41598-018-19449-0>
- [4] E.P. George, D. Raabe, R.O. Ritchie, High-entropy alloys, *Nat. Rev. Mater.* 4 (2019) 515–534, <https://doi.org/10.1038/s41578-019-0121-4>
- [5] W. Li, D. Xie, D. Li, Y. Zhang, Y. Gao, P. Liaw, Mechanical behavior of high-entropy alloys, *Progress in Materials Science* (2021). [10.1016/j.pmatsci.2021.100777](https://doi.org/10.1016/j.pmatsci.2021.100777).
- [6] E. George, W. Curtin, C. Tasan, High entropy alloys: a focused review of mechanical properties and deformation mechanisms, *Acta Mater.* 188 (2020) 435–474, <https://doi.org/10.1016/j.actamat.2019.12.015>, <http://www.sciencedirect.com/science/article/pii/S1359645419308444>.
- [7] Y. Zhang, T.T. Zuo, Z. Tang, M.C. Gao, K.A. Dahmen, P.K. Liaw, Z.P. Lu, Microstructures and properties of high-entropy alloys, *Prog. Mater. Sci.* 61 (2014) 1–93, <https://doi.org/10.1016/j.pmatsci.2013.10.001>
- [8] Y. Lu, X. Gao, L. Jiang, Z. Chen, T. Wang, J. Jie, H. Kang, Y. Zhang, S. Guo, H. Ruan, Y. Zhao, Z. Cao, T. Li, Directly cast bulk eutectic and near-eutectic high entropy alloys with balanced strength and ductility in a wide temperature range, *Acta Mater.* 124 (2017) 143–150, <https://doi.org/10.1016/j.actamat.2016.11.016>, <https://www.sciencedirect.com/science/article/pii/S1359645416308746>.
- [9] M. Wang, Y. Lu, T. Wang, C. Zhang, Z. Cao, T. Li, P.K. Liaw, A novel bulk eutectic high-entropy alloy with outstanding as-cast specific yield strengths at elevated temperatures, *Scr. Mater.* 204 (2021) 114132, <https://doi.org/10.1016/j.scriptamat.2021.114132>, <https://www.sciencedirect.com/science/article/pii/S1359646221004127>.
- [10] B. Cantor, I. Chang, P. Knight, A. Vincent, Microstructural development in equiautomic multicomponent alloys, *Mat. Sci. Eng. A* 375–377 (2004) 213–218, <https://doi.org/10.1016/j.msea.2003.10.257>, <http://www.sciencedirect.com/science/article/pii/S0921509303009936>.
- [11] E.M. Bringa, A. Caro, Y. Wang, M. Victoria, J.M. McNaney, B.A. Remington, R.F. Smith, B.R. Torralva, H. Van Swygenhoven, Ultrahigh strength in nanocrystalline materials under shock loading, *Science* 309 (2005) 1838e1841, <https://doi.org/10.1126/science.1116723>
- [12] K.V. Yusenko, S. Riva, W.A. Crichton, K. Spektor, E. Bykova, A. Pakhomova, A. Tudball, I. Kupenko, A. Rohrbach, S. Klemme, F. Mazzali, S. Margadonna, N.P. Lavery, S.G. Brown, High-pressure high-temperature tailoring of high entropy alloys for extreme environments, *J. Alloy. Compd.* 738 (2018) 491–500, <https://doi.org/10.1016/j.jallcom.2017.12.216>, <http://www.sciencedirect.com/science/article/pii/S0925838817344122>.
- [13] Z.J. Jiang, J.Y. He, H.Y. Wang, H.S. Zhang, Z.P. Lu, L.H. Dai, Shock compression response of high entropy alloys, *Mater. Res. Lett.* 4 (2016) 226–232, <https://doi.org/10.1080/21663831.2016.1191554>
- [14] M. Kawamura, M. Asakura, N.L. Okamoto, K. Kishida, H. Inui, E.P. George, Plastic deformation of single crystals of the equiatomic Cr-Mn-Fe-Co-Ni high-entropy alloy in tension and compression from 10 K to 1273 K, *Acta Mater.* 203 (2021) 116454, <https://doi.org/10.1016/j.actamat.2020.10.073>, <http://www.sciencedirect.com/science/article/pii/S1359645420308715>.
- [15] J.M. Park, J. Moon, J.W. Bae, M.J. Jang, J. Park, S. Lee, H.S. Kim, Strain rate effects of dynamic compressive deformation on mechanical properties and microstructure of CoCrFeMnNi high-entropy alloy, *Mat. Sci. Eng.: A* 719 (2018) 155 – 163, <https://doi.org/10.1016/j.msea.2018.02.031>, <http://www.sciencedirect.com/science/article/pii/S0921509318302156>.
- [16] D. Grady, The spall strength of condensed matter, *J. Mech. Phys. Solids* 36 (1988) 353–384, [https://doi.org/10.1016/0022-5096\(88\)90015-4](https://doi.org/10.1016/0022-5096(88)90015-4)
- [17] T. Remington, B. Remington, E. Hahn, M. Meyers, Deformation and failure in extreme regimes by high-energy pulsed lasers: a review, *Mater. Sci. Eng.: A* 688 (2017) 429–458, <https://doi.org/10.1016/j.msea.2017.01.114>
- [18] E.N. Hahn, T.C. Germann, R.J. Ravelo, J.E. Hammerberg, M.A. Meyers, On the ultimate tensile strength of tantalum, *Acta Mater.* 126 (2017) 313–328, <https://doi.org/10.1016/j.actamat.2016.12.023>
- [19] J. Coakley, A. Higginbotham, D. McGonegle, J. Ilavsky, T.D. Swinburne, J.S. Wark, K.M. Rahman, V.A. Vorontsov, D. Dye, T.J. Lane, S. Boutet, J. Koglin, J. Robinson, D. Milathianaki, Femtosecond quantification of void evolution during rapid material failure, *Sci. Adv.* 6 (2020) eabb4434, <https://advances.sciencemag.org/content/6/51/eabb4434.full>.
- [20] V. Dremov, A. Petrovtsev, P. Sapozhnikov, M. Smirnova, D.L. Preston, M.A. Zocher, Molecular dynamics simulations of the initial stages of spall in nanocrystalline copper, *Phys. Rev. B* 74 (2006) 144110.
- [21] J.P. Escobedo, E.N. Brown, C.P. Trujillo, E.K. Cerreta, G. Gray, The effect of shock-wave profile on dynamic brittle failure, *J. Appl. Phys.* 113 (2013) 103506.
- [22] F. Yuan, L. Chen, P. Jiang, X. Wu, Twin boundary spacing effects on shock response and spall behaviors of hierarchically nanotwinned fcc metals, *J. Appl. Phys.* 115 (2014) 063509.
- [23] S.J. Fensin, S.M. Valone, E.K. Cerreta, J.P. Escobedo-Diaz, G.T. Gray III, K. Kang, J. Wang, Effect of grain boundary structure on plastic deformation during shock compression using molecular dynamics, *Model. Simul. Mater. Sci. Eng.* 21 (2013) 015011.
- [24] Q. An, R. Ravelo, T.C. Germann, W.Z. Han, S.N. Luo, D.L. Tonks, W.A. Goddard III, Shock compression and spallation of single crystal tantalum, *AIP Conf. Proc.* 1426 (2012) 1259–1262.
- [25] C. Li, J. Huang, X. Tang, H. Chai, X. Xiao, Z. Feng, S. Luo, Effects of structural anisotropy on deformation and damage of a duplex stainless steel under high strain rate loading, *Mat. Sci. Eng.: A* 705 (2017) 265 – 272, <https://doi.org/10.1016/j.msea.2017.08.091>, <http://www.sciencedirect.com/science/article/pii/S0921509317311243>.
- [26] S. Zhao, Z. Li, C. Zhu, W. Yang, Z. Zhang, D.E.J. Armstrong, P.S. Grant, R.O. Ritchie, M.A. Meyers, Amorphization in extreme deformation of the CrMnFeCoNi high-entropy alloy, *Sci. Adv.* 7 (2021) eabb3108, <https://doi.org/10.1126/sciadv.eabb3108>
- [27] Z.-C. Xie, C. Li, H.-Y. Wang, C. Lu, L.-H. Dai, Hydrogen induced slowdown of spallation in high entropy alloy under shock loading, *Int. J. Plast.* 139 (2021) 102944, <https://doi.org/10.1016/j.ijplas.2021.102944>, <https://www.sciencedirect.com/science/article/pii/S074964192100019X>.
- [28] N. Gunkelmann, E.M. Bringa, H.M. Urbassek, Influence of phase transition on shock-induced spallation in nanocrystalline iron, *J. Appl. Phys.* 118 (2015) 185902, <https://doi.org/10.1063/1.4935452>
- [29] F. Zhang, H. Lou, B. Cheng, Z. Zeng, Q. Zeng, High-pressure induced phase transitions in high-entropy alloys: A review, *Entropy* 21 (2019) 239, <https://doi.org/10.3390/e21030239>
- [30] W.-H. Liu, Y. Tong, S.-W. Chen, W.-W. Xu, H.-H. Wu, Y.-L. Zhao, T. Yang, X.-L. Wang, X. Liu, J.-J. Kai, C. Liu, Unveiling the electronic origin for pressure-induced phase transitions in high-entropy alloys, *Matter* 2 (2020) 751 – 763, <https://doi.org/10.1016/j.matt.2019.12.023>, <http://www.sciencedirect.com/science/article/pii/S259023851930414X>.
- [31] F. Zhang, H. Lou, S. Chen, X. Chen, Z. Zeng, J. Yan, W. Zhao, Y. Wu, Z. Lu, Q. Zeng, Effects of non-hydrostaticity and grain size on the pressure-induced phase transition of the CoCrFeMnNi high-entropy alloy, *J. Appl. Phys.* 124 (2018) 115901, <https://doi.org/10.1063/1.5046180>
- [32] B. Cao, E. Bringa, M. Meyers, Shock compression of monocrystalline copper: atomistic simulations, *Metall. Mater. Trans. A* 38 (2007) 2681–2688, <https://doi.org/10.1007/s11661-007-9248-9>
- [33] D. Milathianaki, S. Boutet, G.J. Williams, A. Higginbotham, D. Ratner, A.E. Gleason, M. Messerschmidt, M.M. Seibert, D.C. Swift, P. Hering, J. Robinson, W.E. White, J.S. Wark, Femtosecond visualization of lattice dynamics in shock-compressed matter, *Science* 342 (2016) 220–223.
- [34] T. Boehly, R. McCrory, C. Verdon, W. Seka, S. Loucks, A. Babushkin, R. Bahr, R. Boni, D. Bradley, R. Craxton, J. Delettrez, W. Donaldson, R. Epstein, D. Harding, P. Jaanimagi, S. Jacobs, K. Kearney, R. Keck, J. Kelly, T. Kessler, R. Kremens, J. Knauer, D. Lonobile, L. Lund, F. Marshall, P. McKenty, D. Meyerhofer, S. Morse, A. Okishev, S. Papernov, G. Pien, T. Safford, J. Schnittman, R. Short, M.S. III, M. Skeldon, S. Skupsky, A. Schmid, V. Smalyuk, D. Smith, J. Soures, M. Wittman, B. Yaakobi, Inertial confinement fusion experiments with omega-a 30-kj, 60-beam uv laser, *Fusion Eng. Des.* 44 (1999) 35–42, [https://doi.org/10.1016/S0920-3796\(98\)00276-2](https://doi.org/10.1016/S0920-3796(98)00276-2)

- [35] S. Plimpton, Fast parallel algorithms for short-range molecular dynamics, *J. Comput. Phys.* 117 (1995) 1–19, <http://lammps.sandia.gov>.
- [36] W.-M. Choi, Y.H. Jo, S.S. Sohn, S. Lee, B.-J. Lee, Understanding the physical metallurgy of the CoCrFeMnNi high-entropy alloy: an atomistic simulation study, *npj Comput. Mater.* 4 (2018) 1, <https://doi.org/10.1038/s41524-017-0060-9>
- [37] Q. Fang, Y. Chen, J. Li, C. Jiang, B. Liu, Y. Liu, P.K. Liaw, Probing the phase transformation and dislocation evolution in dual-phase high-entropy alloys, *Int. J. Plast.* 114 (2019) 161 – 173, <https://doi.org/10.1016/j.ijplas.2018.10.014>, <http://www.sciencedirect.com/science/article/pii/S0749641918304625>.
- [38] I. Alabd Alhafez, C.J. Ruestes, E.M. Bringa, H.M. Urbassek, Nanoindentation into a high-entropy alloy - an atomistic study, *J. Alloy. Compds.* 803 (2019) 618–624, <https://doi.org/10.1016/j.jallcom.2019.06.277>, <http://www.sciencedirect.com/science/article/pii/S0925838819323679>.
- [39] D.G. Pettifor, Theoretical predictions of structure and related properties of intermetallics, *Mater. Sci. Technol.* 8 (1992) 345–349, <https://doi.org/10.1179/mst.1992.8.4.345>
- [40] B.L. Holian, P.S. Lomdahl, Plasticity induced by shock waves in nonequilibrium MD simulations, *Science* 280 (1998) 2085.
- [41] E.M. Bringa, K. Rosolankova, R.E. Rudd, B.A. Remington, J.S. Wark, M. Duchaineau, D.H. Kalantar, J. Hawreljak, J. Belak, Shock deformation of face-centred-cubic metals on subnanosecond timescales, *Nat. Mater.* 5 (2006) 805.
- [42] A. Stukowski, Visualization and analysis of atomistic simulation data with OVITO - the Open Visualization Tool, *Model. Simul. Mater. Sci. Eng.* 18 (2010) 015012, <http://www.ovito.org>.
- [43] A. Zaddach, C. Niü, C. Koch, D. Irving, Mechanical properties and stacking fault energies of NiFeCrCoMn high-entropy alloy, *Jom* 65 (2013) 1780–1789, <https://doi.org/10.1007/s11837-013-0771-4>
- [44] F. Tian, L.K. Varga, J. Shen, L. Vitos, Calculating elastic constants in high-entropy alloys using the coherent potential approximation: current issues and errors, *Comput. Mater. Sci.* 111 (2016) 350–358, <https://doi.org/10.1016/j.commatsci.2015.09.058>
- [45] H. Ge, H. Song, J. Shen, F. Tian, Effect of alloying on the thermal-elastic properties of 3d high-entropy alloys, *Mater. Chem. Phys.* 210 (2018) 320–326, <https://doi.org/10.1016/j.matchemphys.2017.10.046>
- [46] S. Huang, A. Vida, A. Heczel, E. Holmström, L. Vitos, Thermal expansion, elastic and magnetic properties of FeCoNiCu-based high-entropy alloys using first-principle theory, *JOM* 69 (2017) 2107–2112, <https://doi.org/10.1007/s11837-017-2565-6>
- [47] J.W. Wilkerson, K.T. Ramesh, Unraveling the anomalous grain size dependence of cavitation, *Phys. Rev. Lett.* 117 (2016) 215503, <https://doi.org/10.1103/PhysRevLett.117.215503>
- [48] M.A. Meyers, *Dynamic Behavior of Materials*, John Wiley & Sons, Ltd, 1994.
- [49] Y. Qi, X. Chen, M. Feng, Molecular dynamics-based analysis of the effect of temperature and strain rate on deformation of nanocrystalline CoCrFeMnNi high-entropy alloy, *Appl. Phys. A* 126 (2020) 529, <https://doi.org/10.1007/s00339-020-03714-z>
- [50] C.E. Wehrenberg, D. McGonegle, C. Bolme, A. Higginbotham, A. Lazicki, H.J. Lee, B. Nagler, H.-S. Park, B.A. Remington, R.E. Rudd, M. Sliwa, M. Suggit, D. Swift, F. Tavella, L. Zepeda-Ruiz, J.S. Wark, In situ x-ray diffraction measurement of shock-wave-driven twinning and lattice dynamics, *Nature* 550 (2017) 496–499, <https://doi.org/10.1038/nature24061>
- [51] S.-N. Luo, Q. An, T.C. Germann, L.-B. Han, Shock-induced spall in solid and liquid Cu at extreme strain rates, *J. Appl. Phys.* 106 (2009) 013502.
- [52] A. Stukowski, Structure identification methods for atomistic simulations of crystalline materials, *MSMSE* 20 (2012) 045021.
- [53] G. Righi, C.J. Ruestes, C.V. Stan, S.J. Ali, R.E. Rudd, M. Kawasaki, H.-S. Park, M.A. Meyers, Towards the ultimate strength of iron: spalling through laser shock, *Acta Mater.* 215 (2021) 117072, <https://doi.org/10.1016/j.actamat.2021.117072>
- [54] T. Remington, E. Hahn, S. Zhao, R. Flanagan, J. Mertens, S. Sabbaghianrad, T. Langdon, C. Wehrenberg, B. Maddox, D. Swift, B. Remington, N. Chawla, M. Meyers, Spall strength dependence on grain size and strain rate in tantalum, *Acta Mater.* 158 (2018) 313–329, <https://doi.org/10.1016/j.actamat.2018.07.048>, <http://www.sciencedirect.com/science/article/pii/S1359645418305846>
- [55] H.-T. Luu, R.J. Ravelo, M. Rudolph, E.M. Bringa, T.C. Germann, D. Rafaja, N. Gunkelmann, Shock-induced plasticity in nanocrystalline iron: Large-scale molecular dynamics simulations, *Phys. Rev. B* 102 (2020) 020102, <https://doi.org/10.1103/physrevb.102.020102>
- [56] D.A. Indeitsev, A.M. Krivtsov, P.V. Tkachev, Molecular dynamics analysis of the relation between the spall strength and strain rate for solids, *Dokl. Phys.* 51 (2006) 154–156, <https://doi.org/10.1134/S1028335806030141>
- [57] S. Galitskiy, D. Ivanov, A. Dongare, Dynamic evolution of microstructure during laser shock loading and spall failure of single crystal al at the atomic scales, *J. Appl. Phys.* 124 (2018) 205901, <https://doi.org/10.1063/1.5051618>